# Resilience through diversity: Loss of neuronal heterogeneity in epileptogenic human tissue renders neural networks more susceptible to sudden changes in synchrony

Scott Rich[1,*], Homeira Moradi Chameh[1], Jeremie Lefebvre[1,2,3,†], and Taufik A Valiante[1,4,5,6,7,†]

[1]Krembil Research Institute, University Health Network (UHN), Division of Clinical and Computational Neuroscience, Toronto, Ontario, Canada

[2]University of Ottawa, Department of Biology, Ottawa, Ontario, Canada

[3]University of Toronto, Department of Mathematics, Toronto, Ontario, Canada

[4]University of Toronto, Institute of Biomedical Engineering, Toronto, ON, Canada

[5]University of Toronto, Electrical and Computer Engineering, Toronto, ON, Canada

[6]University of Toronto, Institute of Medical Science, Toronto, ON, Canada

[7]University of Toronto, Division of Neurosurgery, Department of Surgery, Toronto, ON, Canada

[*]Corresponding Author: scott.rich@uhnresearch.ca

[†]These authors share senior authorship of this work.

March 2, 2021

**Abstract**

A myriad of pathological changes associated with epilepsy can be recast as decreases in cell and circuit heterogeneity. We propose that epileptogenesis can be recontextualized as a process where reduction in cellular heterogeneity renders neural circuits less resilient to transitions into information-poor, over-correlated seizure states. We provide *in vitro*, *in silico*, and mathematical support for this hypothesis. Patch clamp recordings from human layer 5 (L5) cortical neurons demonstrate significantly decreased biophysical heterogeneity of excitatory neurons in seizure generating areas (epilepetogenic zone). This decreased heterogeneity renders model neural circuits prone to sudden dynamical transitions into synchronous, hyperactive states (paralleling ictogenesis) while also explaining counter-intuitive differences in population activation functions (i.e., FI curves) between epileptogenic and non-epileptogenic tissue. Mathematical analyses based in mean-field theory reveal clear distinctions in the dynamical structure of networks with low and high heterogeneity, providing the theoretical undergird for how ictogenic dynamics accompany a reduction in biophysical heterogeneity.

# Introduction

Epilepsy, the most common serious neurological disorder in the world [1], is characterized by the brain's proclivity for seizures, which exhibit highly correlated electrophysiological activity and elevated neuronal spiking [2]. While the etiologies that predispose the brain to epilepsy are myriad [3], the dynamics appear to be relatively conserved [4, 5], suggesting a small palette of candidate routes to the seizure state. One potential route to ictogenesis is disruption of excitatory/inhibitory balance (EIB) - a possible "final common pathway" for various epileptogenic etiologies, and a fundamental motivation for decades of basic science research into epilepto- and ictogenesis [6, 7]. A disrupted EIB can result in the loss of resilience of neural circuits to correlated inputs [8], a paramount characteristic of ictogenesis. In addition to EIB, biophysical heterogeneity also provides resilience to correlated inputs [9]. Thus, EIB can be considered a synaptic mechanism for input decorrelation, while biophysical heterogeneity contributes to decorrelation post-synaptically.

Cellular heterogeneity is the norm, not the exception, in biological systems [10, 11]. In the brain, experimental and theoretical work has demonstrated that such variability greatly expands the informational content of neural circuits, in part by reducing correlated neuronal activity [12, 13]. Since heightened levels of firing and firing rate correlations hallmark seizures [4, 14], we hypothesize that epilepsy may be likened, in part, to pathological reductions in biological heterogeneity which impair decorrelation, and thus circuit resilience to transitioning to information poor [15], high-firing [2], and highly-correlated states [14].

Although not previously studied through the lens of neural homogenization, a number of pathological changes accompanying epileptogenesis and epilepsy can be recast as decreases in biological heterogeneity.

Losses of specific cell-types homogenize neural populations [16, 17], down- or upregulation of ion channels in acquired and genetic epilepsies homogenize biophysical properties [18–20], and synaptic sprouting homogenizes neural inputs [21]. This recontextualizes epileptogenesis as a process associated with the progressive loss of biophysical heterogeneity.

To explore this hypothesis we combine electrophysiological recordings from human cortical tissue, computational modeling, and mathematical analysis to detail the existence and subsequent consequences of one type of reduction in biological variability in epilepsy: the decrease of intrinsic neuronal heterogeneity. We first provide experimental evidence for decreased biophysical heterogeneity in neurons within brain regions that generate seizures (epileptogenic zone) when compared to non-epileptogenic regions. We use this biological information to explore the effects of heterogeneity in neural excitability on simulated brain circuits. Using a cortical excitatory-inhibitory (E-I) spiking neural network, we show that networks with neuronal heterogeneity mirroring epileptogenic tissue are more vulnerable to sudden shifts from an asynchronously firing state to a hyperactive synchronous state, which has clear parallels with seizure onset. Meanwhile, networks with neuronal heterogeneity mirroring non-epileptogenic tissue are more resilient to such transitions and exist more stably in the asynchronous state. These differing heterogeneity levels also underlie the significant, yet counter-intuitive, differences in the neural activation functions (i.e., frequency-current or FI curves) measured inside and outside the epileptogenic zone. Using mean-field analysis, we show that differences in the predisposition towards a sudden shift into synchrony and activation functions are both consequences of varying degrees of neuronal diversity. Viewed together, our experimental, computational, and mathematical results strongly support the hypothesis that biophysical heterogeneity enhances the dynamical resilience of neural networks while explaining how reduced diversity can predispose circuits to seizure initiation.

# Results

## Intrinsic biophysical heterogeneity is reduced in human epileptogenic cortex

In search of experimental evidence for reduced biophysical heterogeneity in brain regions generating seizures, we utilized the rare access to live human cortical tissue obtained during resective epilepsy surgery. Whole-cell current clamp recordings characterized the passive and active properties of layer 5 (L5) pyramidal cells from these cortical samples, a cell type we have previously shown to display notable biophysical heterogeneity [22]. Biophysical properties of neurons from epileptogenic frontal lobe cortex were contrasted to frontal lobe neurons of patients with no previous history of seizures undergoing tumor resection. Additionally, we obtained recordings from neurons in non-epileptogenic middle temporal gyrus (MTG) from patients with mesial

temporal sclerosis, which is the overlying cortex routinely removed to approach deep temporal structures. The MTG is a well-characterized part of the human brain, representing a common anatomical region from which non-epileptogenic brain tissue has been studied electrophysiologically and transcriptomically [22–25], and thus our primary source of non-epileptogenic neurons.

Our analysis concentrated on two critical electrophysiological features characterizing cellular excitability. The first was the distance to threshold (DTT) measured as the difference between the resting membrane potential (RMP) and rheobase (i.e., firing threshold) of these neurons. Whole-cell recordings revealed less DTT variability (smaller coefficient of variation (CV); p=0.04, two sample coefficient of variation test) in epileptogenic frontal lobe (n=13, CV=20.3%) as compared to non-epileptogenic MTG (n=77, CV=37.1%). A significant difference (smaller CV; p=0.03, two sample coefficient of variation test) was also seen when comparing epileptogenic frontal lobe to non-epileptogenic frontal lobe (n=12, CV=40.8%). Meanwhile, the CVs were not significantly different when comparing non-epileptogenic MTG and non-epileptogenic frontal lobe (p=0.7, two sample coefficient of variation test). These features are more easily appreciated from the Gaussian fits of this data presented in Figure 1**(b)**; all three data sets were deemed normal after passing both the Shapiro-Wilk and D'Agostino & Pearson omnibus normality tests with alpha=0.05. These experimental results reveal that, regardless of the anatomical location from which non-epileptogenic tissue was removed for comparison to epileptogenic frontal lobe, biophysical heterogeneity was decreased in epileptogenic cortex. A standard threshold of $p<0.05$ is used to report statistically significant differences.

Our second primary quantification of cellular excitability was the FI curve (i.e., activation function), which captures the firing rate (F) as function of input current (I). We experimentally measured firing rates of neurons as the input current was increased from 50 to 250 pA in 50 pA steps. The resulting activation function of the population of neurons within the epileptogenic zone displayed both qualitative and quantitative differences compared to neurons from non-epileptogenic cortex, be it from MTG or frontal lobe (Figure 1**(c)**). Surprisingly, firing threshold was found to be higher in the epileptogenic zone compared to both non-epileptogenic populations. Additionally, firing rates were significantly lower in the epileptogenic zone (p=0.03 when comparing epileptogenic frontal lobe to non-epileptogenic frontal lobe at 200 pA, p=0.02 when comparing epileptogenic frontal lobe to non-epileptogenic frontal lobe at 250 pA, p=0.009 when comparing epileptogenic frontal lobe to non-epileptogenic MTG at 200 pA, and p=0.002 when comparing epileptogenic frontal lobe to non-epileptogenic MTG at 250 pA; two-way ANOVA-Tukey's multiple comparison test), indicating larger inputs are required to induce high-frequency repetitive firing in individual neurons from epileptogenic tissue. This non-linear behavior is in strong contrast to the activation functions measured in non-epileptogenic zones, characterized by both higher and more linear changes in firing rates. This increased excitability of the non-epileptogenic populations appears contradictory to the understanding of seizure as a

hyperactive brain state, a seemingly paradoxical finding further investigated in the context of biophysical heterogeneity in the following.

## Spiking E-I neural networks with epileptogenic levels of excitatory heterogeneity are more vulnerable to sudden changes in synchrony

Given these confirmatory experimental results, we next explored the effects of biophysical heterogeneity on the transition to a synchronous state akin to the transition to seizure [14]. We developed a spiking network model of a cortical microcircuit comprised of recurrently connected excitatory and inhibitory neurons (see details in Methods), motivated in part by the long history of seizure modeling [4, 26] and previous models of decorrelated activity in the cortex [8, 27, 28]. We tuned our network model parameters (see details in Methods) to position the system near a tipping point at which synchronous activity arises [29–31] in order to characterize the transition from decorrelated to synchronous activity, similar to our previous work [32]. Following the conventions of bifurcation analysis [33], we subjected these networks to a slowly linearly increasing external drive to the excitatory cells. This allows us to analyze the stability of the asynchronous state, known to be the physiological state of the cortex [8, 27, 28], by determining how vulnerable the network is to a bifurcation forcing the system out of this dynamic and into a state of increased synchrony and firing. A biological analogue for this paradigm would be an examination of whether induced hyper-excitability might drive the onset of seizure-like activity *in vitro*, although such perturbations can more easily be performed continuously (i.e., our linearly increasing external drive) rather than discretely (i.e., inducing hyper-excitability pharmacologically) *in silico*.

To facilitate the direct implementation of experimentally-derived heterogeneities in our model, we compared epileptogenic frontal lobe with non-epileptogenic MTG given their similar mean DTT values (p=0.7, non-parametric Mann-Whitney test; mean=21.2 mV for non-epileptogenic MTG and mean=21.7 mV for epileptogenic frontal lobe). Along with the significantly different CV values discussed above, these populations also display significantly different standard deviations (SD; p=0.03, F-test; SD=7.8 mV in non-epileptogenic MTG and SD=4.4 mV in epileptogenic frontal lobe). Given the mathematical conventions of our neuron model (specifically, rheobases sampled from a normal distribution with with mean 0, see details in Methods), we implement differing heterogeneities by sampling rheobase values for our neural populations from Gaussian distributions with these varying SDs. Given the linear relationship between the rheobase and the DTT (see above), rheobase heterogeneity is the *in silico* analogue of the experimentally observed heterogeneity in the DTT (i.e., the distribution of neural rheobases in Figure 2**(c-d)** is approximately a horizontal shift to a mean of 0 of the DTT distributions in Figure 1**(b)**).

The heterogeneity in the rheobase was parameterized by the standard deviations $\sigma_e$ for the excitatory population and $\sigma_i$ for the inhibitory population (see diagrams in Figure 2**(a-b)**). Such heterogeneity results in diversity in the neurons' activation functions and aligns the variability in their excitabilities with that measured experimentally. We refer to such rheobase heterogeneity simply as heterogeneity in the remainder of the text.

Model networks with epileptogenic (high $\sigma_e = 7.7$ mV, Figure 2**(e)**) and non-epileptogenic (low $\sigma_e = 4.4$ mV, Figure 2**(f)**) excitatory heterogeneity with identical, moderate inhibitory heterogeneity ($\sigma_i = 10.0$ mV) exhibit distinct behaviors. With low excitatory heterogeneity, a sharp, non-linear increase in excitatory synchrony and firing rates of both populations was observed. Indeed, firing activity transitioned abruptly from quiescent to fully synchronous. In contrast, when the excitatory heterogeneity was high, both synchrony and firing rates scaled linearly with input amplitude.

We further investigated the respective roles of excitatory versus inhibitory heterogeneity in generating these sudden transitions. With non-epileptogenic amounts of excitatory heterogeneity (high $\sigma_e$), increases in excitatory synchrony, excitatory firing rates, and inhibitory firing rates were all largely linear regardless of whether $\sigma_i$ was low (Figure 3**(a)**) or high (Figure 3**(b)**), although the overall level of synchrony was decreased with high $\sigma_i$. Conversely, with excitatory heterogeneity reflective of epileptogenic cortex (low $\sigma_e$), synchronous transitions were observed for both low (Figure 3**(c)**) and high (Figure 3**(d)**) levels of $\sigma_i$. However, there are key differences between these transitions: the sudden increase in synchrony is coupled with a similarly abrupt increase in both excitatory and inhibitory firing rates with low $\sigma_i$ but not high $\sigma_i$. This difference is indicative of the differing underlying dynamical structures of these networks which we elucidate below.

## Dynamical differences in networks with varying levels of heterogeneity are explained by their distinct mathematical structures

Firing rates and synchrony measures averaged over 10 independent realizations (Figure 4, top row) revealed minimal variability in the dynamics and preservation of the transitions seen in Figure 3, suggesting that these dynamics are robust and reproducible. To gain deeper insight into these dynamics at a potential transition to synchrony, we derived and analyzed mathematically the mean-field equations associated with our network model (see Methods). Specifically, we calculated and classified the fixed points of mean-field equations for different values of $\sigma_e$ and $\sigma_i$ over the range of excitatory inputs studied in the spiking networks. The fixed point values of the mean excitatory activity are plotted in the second row of each panel in Figure 4. The dampening rate, which represents the speed at which the system is either repelled from or returns to its fixed point(s) and classifies their stability, is plotted in the next row of Figure 4, followed by the frequency of any

oscillatory fixed points.

Most interestingly, the mathematical properties of the network with both low $\sigma_e$ and $\sigma_i$ (Figure 4**(c)**) are entirely unique from scenarios where one or both of these heterogeneity values is high. In the low-heterogeneity setting, multiple fixed points exist at the lowest values of the external drive until only an unstable oscillatory fixed point remains. Notably, the value of the drive at which this bifurcation occurs is in agreement with the value of the drive at which we see the sudden shift in dynamics in spiking networks (compare top two panels of Figure 4**(c)**). Thus, decreased neural heterogeneity in both the excitatory and inhibitory populations results in multi-stability and a bifurcation that is responsible for the sudden transition to synchrony. The mathematical analysis also sheds light on other, subtle differences in the network dynamics driven by varying levels of excitatory and inhibitory heterogeneity (specifically the difference in the transitions seen in Figure 4**(c)** and **(d)**, see Discussion).

## Asymmetric effects of excitatory and inhibitory heterogeneity

To clarify the seeming disparate influence of excitatory versus inhibitory variability on the onset of synchrony, we systematically explored the effect of heterogeneity on network dynamics over a larger parameter space (Figure 5). For each heterogeneity combination we computed the Bifurcation Measure $B$, which quantifies changes in synchrony over time (see details in Methods) and is thus an indirect metric for the presence of sudden transitions. From this visualization, we can draw three important conclusions: first, $B$ achieves its highest values when both $\sigma_e$ and $\sigma_i$ are at their lowest, a regime which includes networks with the low $\sigma_e$ value aligned with experimental data from epileptogenic tissue; second, $B$ decreases abruptly as $\sigma_e$ increases, with $\sigma_i$ having minimal effect on $B$ for high values of $\sigma_e$; third, $B$ decays more slowly as $\sigma_i$ is increased, with $\sigma_e$ retaining some effect on $B$ for high values of $\sigma_i$.

The bold border in Figure 5**(a)** delimits heterogeneity combinations in the parameter space supporting multi-stability in the mean-field analysis (bottom-left) from those that exclusively exhibit a single fixed point. This demarcation reflects network dynamics with the highest values of $B$ while matching the asymmetric effect of $\sigma_e$ and $\sigma_i$. We show an example visualization of the fixed points and their classifications for one input current yielding multi-stability in Supplementary Figure S1. In Supplementary Figure S2 we further show the pattern followed by $B$ is robust to changes in connectivity density. These conclusions support an asymmetric effect of excitatory versus inhibitory heterogeneity and confirm our findings from Figure 4.

In order to further describe the predictive relationship between the results of spiking network simulations and mean-field analyses, we explore the dynamical features of networks when subjected to a constant input current. In Figure 5**(b-c)** we quantify the excitatory synchrony and firing rate for each network in the

parameter space when stimulated by a constant input current (see details in Methods). The bold border demarcates regions in the parameter space where the mean-field equations yield an unstable fixed point (bottom-left) from those with a stable fixed point (top-right), with the details of this analysis shown in Supplementary Figure S3. The region with an unstable fixed point corresponds with the occurrence of strongest network synchrony and the most homogeneous networks, a relatively small portion of our parameter space. This finding further supports the correspondence between our mean-field analysis and the behavior of our spiking networks, and the ability of such analysis (here via the stability of the fixed point) to make predictions regarding spiking network dynamics.

This analysis also allows us to more directly compare the dynamics of our networks with results from previous literature. For instance, for set values of $\sigma_e$, networks that fire more synchronously (Figure 5**(b)**) also tend to fire at higher frequencies (Figure 5**(c)**), a result that builds upon a similar understanding from purely inhibitory networks [34, 35] and mirrors electrophysiological signatures of ictogenesis [2, 36]. Such comparisons are further expounded upon in the Discussion.

The differences between the patterns displayed by $B$ (Figure 5**(a)**) and the Synchrony Measure (Figure 5**(b)**) are illustrative. In networks in which one, but not both, of the heterogeneity values are high, networks driven by a constant input can exhibit similar, relatively high synchrony levels. However, the differences in these networks' predisposition towards a sudden transition into said synchrony are revealed through differing values of $B$ (compare the bottom-right and top-left corners of the heatmaps in Figure 5**(a-b)**). This underlies our focus on how differing heterogeneities affect mathematical bifurcations and the corresponding sudden transitions in network dynamics (encapsulated by $B$) rather than steady-state network dynamics, especially in the context of studying seizure onset.

## Differences in population averaged activation functions explained by differences in neural heterogeneity

Finally, we return to the counter-intuitive differences in activation functions measured experimentally. As noted previously, the population of neurons from epileptogenic tissue exhibited qualitatively and quantitatively different activation functions: epileptogenic zone neurons exhibited non-linear and low frequency firing responses when compared to neurons from non-epileptogenic tissue (Figure 1**(c)**).

To understand if heterogeneity could account for these observations, we computed analytically the averaged activation functions of the excitatory populations in our model networks, taking into account the rheobase heterogeneity. In Figure 6**(a)**, the experimentally derived firing frequencies from epileptogenic frontal lobe and non-epileptogenic MTG are plotted alongside activation functions for our model populations. For low

heterogeneity, the model population's activation function captured both the non-linear and low firing rate responses measured experimentally for neurons in the epileptogenic zone. The increased excitability and linearity seen experimentally in non-epileptogenic tissue was captured by the averaged activation function for our more heterogeneous model population.

To quantitatively support for this this qualitative correspondence, we found the values of $\sigma_e$ that best fit our experimental data using a non-linear least squares method (see details in Methods). The data from epileptogenic frontal lobe was best fit by an activation function (see Equation 12) with $\sigma_e = 5.039$ mV ($r^2$=0.9363), while the data from non-epileptogenic MTG was best fit by an activation function with $\sigma_e = 7.771$ mV ($r^2$=.9840). These best-fit values closely match the experimentally-observed heterogeneity values and more quantitatively show that the features of our epileptogenic (resp. non-epileptogenic) activation curves are captured by neural populations with low (resp. high) heterogeneity.

This somewhat counter-intuitive result is explained by the linearizing effect that increased heterogeneity, and noise more generally, has on input-output response functions [37, 38]. This effect is illustrated in Figure 6**(b)**. The bolded sigmoids, of which the portion highlighted by a grey box was compared to experimental data in Figure 6**(a)**, represent the averaged activity of the entire population of heterogeneous neurons alongside individual activation functions (fainter sigmoids). Increased (resp. decreased) variability dampens (resp. sharpens) the averaged response curve for the non-epileptogenic (resp. epileptogenic) setting. In particular, such variability-induced linearization raises the excitability at low input values, corresponding with the dynamics highlighted in Figure 6**(a)**. The results of Figure 6 illustrate that our model predicts significant differences in the activation function between epileptogenic and non-epileptogenic tissue, and that heterogeneity, or lack thereof, can explain counter-intuitive neuronal responses. In turn, this shows the hyper-excitability associated with seizure activity is *not* necessarily associated with increased excitability as represented by a lower firing threshold or higher firing rate of individual neurons.

# Discussion

In this work, we propose that neural heterogeneity serves an important role in imparting neural circuits with a resilience to epileptogenesis, and correspondingly that its loss may be a "final common pathway" for a number of etiologies that are associated with epilepsy. We explored this hypothesis using *in vitro* electrophysiological characterization of human cortical tissue from epileptogenic and non-epileptogenic areas, which revealed significant differences in DTT (a key determinant of neuronal excitability) heterogeneity in the pathological and non-pathological settings. The ability to perform experiments on tissue from human subjects diagnosed with epilepsy makes these results particularly relevant to the human condition. We then

implemented these experimentally observed heterogeneities in an analogous parameter in *in silico* spiking neural networks. Our explorations show that networks with high heterogeneity, similar to the physiological setting, exhibit a more stable asynchronously firing state that is resilient to sudden transitions into a more active and synchronous state. Differing heterogeneity levels also explained the significant differences in the experimentally-obtained population activation function between epileptogenic and non-epileptogenic tissue. Finally, using mathematical analysis we show that differences in the stability of analogous mean-field systems provide a theoretical explanation for the dynamical differences observed in spiking networks. Viewed jointly, these three avenues of investigation provide strong evidence that reduction in biophysical heterogeneity *exists* in epileptogenic tissue, can *yield dynamical changes* with parallels to seizure onset, and that there are *fundamental mathematical/theoretical principles* underlying these differences.

Computational studies have established the role played by heterogeneity in reducing synchronous activity in the context of physiological gamma rhythms [39–41]. Other computational investigations have implemented heterogeneity in more varied neural parameters [42] and identified asymmetric effects of excitatory and inhibitory heterogeneities on network dynamics [37,43]. Our study complements and extends the understanding of the role of biophysical heterogeneity in neural networks to the real world problem of human epilepsy by: 1) using experimentally derived heterogeneities of the DTT in non-epileptogenic and epileptogenic surgical specimens, which when implemented *in silico* are dynamically relevant; 2) exploring the effects of heterogeneity on the transition to synchrony, the hallmark of seizure onset; 3) detailing the differing extents to which inhibitory and excitatory heterogeneity contribute to circuit resilience to synchronous transitions. Our mathematical analysis further builds on this work to provide a theoretical undergird for these observed dynamics.

The asymmetrical effect of excitatory and inhibitory heterogeneities is interesting, and our work allows us to make computationally and mathematically supported predictions regarding the effects of inhibitory heterogeneity on ictogenesis. Figure 5**(a)** shows that increasing $\sigma_i$ leads to a more gradual decrease in $B$ than increasing $\sigma_e$, meaning that sudden transitions are more likely to arise for moderate values of $\sigma_i$ than $\sigma_e$. The physiological heterogeneity of the entire inhibitory population in a cortical microcircuit is likely to be larger than for the excitatory population [44], driven in part by the diverse subpopulations of interneurons [45]. Thus, our work makes two interesting predictions: first, the homogenization or loss of just one of these subpopulations might be sufficient to make a system more vulnerable to ictogenesis (as such transitions arise at larger values of $\sigma_i$ than $\sigma_e$ in our model); second, the preservation of inhibitory heterogeneity may provide a bulwark against ictogenesis even if excitatory heterogeneity is pathologically reduced as we observed experimentally.

While we did not characterize the levels of heterogeneity in inhibitory neurons, the loss of individual

inhibitory cell types [16, 17] or unique firing patterns within the population of inhibitory cells [46] previously shown to be associated with epilepsy can be thought of as a loss of inhibitory heterogeneity. These studies tend to contextualize the epileptogenic effect of these changes as driven by a deficit in GABAergic signalling, either due to the loss of inhibitory cells [17] (or, in the case of Cossart et. al. [16], the loss of specifically dendritic targeting inhibitory signaling) or to fewer action potentials generated by inhibitory cells [46]. We present a potential additional route to the seizure state under such conditions, where the loss of inhibitory neuronal heterogeneity promotes ictogenesis, which could serve to reconcile these studies' sometimes conflicting observations regarding the loss of interneurons.

From a mathematical perspective, Figure 4**(c-d)** displays two distinct pathways by which our model networks can achieve a more synchronously firing state. In Figure 4**(c)** this transition is sudden and occurs alongside a sudden increase in excitatory and inhibitory firing rates. Mean-field analysis reveals a saddle-node bifurcation [33], as the two purely real fixed points coalesce and disappear, leaving only the oscillatory fixed point. In contrast, in Figure 4**(d)** excitatory synchrony arises more gradually, and critically the most obvious "jumps" in synchrony do not correspond with sudden increases in excitatory activity. Here, mean-field analysis reveals a transition of the lone fixed point from a stable to unstable oscillator, which is denoted a Hopf bifurcation [33]. Since the seizure state is typified both by increased synchrony and firing rates [2, 14], this analysis indicates that the transition driven by a saddle-node bifurcation (Figure 4**(c)**) is more similar to physiologically observed seizure onset. These behaviors are in line with seizure modeling studies showcasing that ictogenic transitions can arise driven by mathematical bifurcations, and specifically the observation that saddle-node bifurcations underlie abrupt seizure-onset dynamics [4, 5, 26].

While our results include lower neuronal counts from the frontal lobe, frontal lobe from individuals with seizures and from tumor patients represent much less common sources of human cortical tissue than non-epileptogenic MTG. Although one might obtain a greater sample by comparing non-epileptogenic MTG to epileptogenic mesial temporal structures (i.e., subiculum, parahippocampal gyrus, hippocampus) this would represent comparison between the allocortex and neocortex which would add a further confound given the potential for differing levels of healthy biophysical heterogeneity between these regions. Alternatively, obtaining non-epileptogenic medial temporal lobe (MTL) cortex is exceedingly rare. With these important limitations in the access to human cortical tissue considered, our comparison between epileptogenic frontal lobe, non-epileptogenic (tumor) frontal lobe, and non-epileptogenic MTG represent a best-case comparison of the biophysical properties of epileptogenic and non-epileptogenic human tissue while reasonably controlling for confounds introduced by the differing brain regions.

Our model networks, while analogous to E-I micro-circuits commonly used in computational investigations of cortical activity [8, 27, 28], are simplified from the biophysical reality and must be considered with these

limitations in mind; indeed, such models cannot reasonably capture the full richness and complexity of seizure dynamics and do not include multiple inhibitory populations [45]. However, this simplifying choice facilitates findings that have their foundation in fundamental mathematical principles and are not especially reliant on biophysical intricacies such as network topology (see the Supplementary Material of Rich et. al. [32]). This increases the likelihood that these predictions are generalizable. Potential future work involves the use of more biophysically detailed neuron and network models, allowing for the implementation and study of additional types of heterogeneity (including multiple, diverse inhibitory populations) and/or the study of model seizures. Such studies will be facilitated by our recent development of a biophysically-detailed computational model of a human L5 cortical pyramidal neuron [47], allowing them to be more directly applicable to the human brain and potential clinical applications for the treatment of patients with epilepsy.

In this vein, while we do not model seizures per se in this work, the two most commonly observed types of seizure onsets observed in intracranial recordings are the the low-voltage fast [48] and hyper-synchronous onsets [49]. Both of these transitions reflect a sudden transition from a desynchronized state to a synchronous oscillation, albeit of differing frequencies. Given the ubiquity of such oscillatory onsets, our modelling of the transition to synchrony is likely to be broadly relevant to epilepsy.

Lastly, one might wonder what neurobiological processes render an epileptogenic neuronal population less biophysically diverse. While it is well accepted that under physiological conditions, channel densities are regulated within neurons to obtain target electrical behaviors [50], it remains speculative as to what processes might lead to the pathological homogenization of neuronal populations. However, computational modeling suggests that biological diversity may be a function of input diversity, and thus "homogenizing the input received by a population of neurons should lead the population to be less diverse" [13]. Although requiring further exploration, it is possible that the information-poor, synchronous post-synaptic barrages accompanying seizure [15] represent such a homogenized input, reducing a circuit's resilience to synchronous transitions and promoting epileptogenesis by reducing biophysical heterogeneity.

# Acknowledgments

We thank Frances Skinner, Shreejoy Tripathy, Prajay Shah and Anukrati Nigam for productive intellectual discussions on this topic in the project's early stages. We thank the National Research Council of Canada (NSERC Grants RGPIN-2017-06662 to J.L. and RGPIN-2015-05936 to T.A.V.), the Krembil Foundation (Krembil Seed Grant to J.L. and T.A.V.), and the University of Toronto Department of Physiology (Yuet Ngor Wong Award to S.R.) for support of this research.

# Author Contributions

Conception and design of the work: SR, HMC, JL, TAV. Experimental data collection: HMC. Data analysis and interpretation: SR, HMC, TAV. Simulations: SR. Mathematical analysis: SR, JL. Initial drafting of article: SR. Article edits and revisions: SR, HMC, JL, TAV. All authors gave final approval of the version to be submitted.

# Competing Interests

The authors have no competing interests.

# Materials and Methods

The research presented here analyzes the role of neural heterogeneity using biological experiment, computational modeling, and mathematical analysis. The details of the experiments are found below, followed by the details of the two models used in the computational portion of this work, a spiking excitatory-inhibitory (E-I) neural network model and mean-field analyses of analogous Wilson-Cowan style population models.

## Experiment

### Human brain slice preparation

All procedures on human tissue were performed in accordance with the Declaration of Helsinki and approved by the University Health Network Research Ethics board. Patients underwent a standardized temporal or frontal lobectomy [51] under general anesthesia using volatile anesthetics for seizure treatment [52]. Tissue was obtained from patients diagnosed with temporal or frontal lobe epilepsy who provided written consent. Tissue from temporal lobe was obtained from 22 patients, age ranging between 21 to 63 years (mean age $\pm$ SEM: $37.8 \pm 2.9$). The resected temporal lobe tissue displayed no structural or functional abnormalities in preoperative MRI and was deemed "healthy" tissue considering it is located outside of the epileptogenic zone. Tissue from frontal lobe was obtained from five patients, age ranging between 23-36 years (mean age $\pm$ SEM: $30.2 \pm 2.4$), and was deemed "epileptogenic" tissue as it was obtained from the epileptogenic zone. Tissue from non-epileptogenic frontal lobe obtained during tumor resection was obtained from two patients, age ranging between 37-58 years (mean age $\pm$ SEM: $47.5 \pm 10.5$), and was also considered "non-epileptogenic".

After surgical resection, the cortical tissue block was instantaneously submerged in ice-cold ($\sim$4°C) cutting solution that was continuously bubbled with 95% $O_2$-5% $CO_2$ containing (in mM): sucrose 248, KCl 2,

$MgSO_4.7H_2O$ 3, $CaCl_2.2H_2O$ 1, $NaHCO_3$ 26, $NaH_2PO_4.H_2O$ 1.25, and D-glucose 10. The osmolarity was adjusted to 300-305 mOsm. The human tissue samples were transported (5-10 min) from Toronto Western Hospital (TWH) to the laboratory for further slice processing. Transverse brain slices (400 $\mu$m) were obtained using a vibratome (Leica 1200 V) perpendicular to the pial surface to ensure that pyramidal cell dendrites were minimally truncated [52, 53] in the same cutting solution as used for transport. The total duration, including slicing and transportation, was kept to a maximum of 20-30 minutes. After sectioning, the slices were incubated for 30 min at 34°C in standard artificial cerebrospinal fluid (aCSF) (in mM): NaCl 123, KCl 4, $CaCl_2.2H_2O$ 1, $MgSO_4.7H_2O$ 1, $NaHCO_3$ 26, $NaH_2PO_4.H_2O$ 1.2, and D-glucose 10. The pH was 7.40 and after incubation the slice was held for at least for 60 min at room temperature. aCSF in both incubation and recording chambers were continuously bubbled with carbogen gas (95% $O_2$-5% $CO_2$) and had an osmolarity of 300-305 mOsm.

**Electrophysiological recordings and intrinsic physiology feature analysis**

For recordings, slices were transferred to a recording chamber mounted on a fixed-stage upright microscope (Axioskop 2 FS MOT; Carl Zeiss, Germany). Recordings were performed from the soma of pyramidal neurons at 32-34° in recording aCSF continually perfused at 4 ml/min. Cortical neurons were visualized using an IR-CCD camera (IR-1000, MTI, USA) with a 40x water immersion objective lens. Using the IR-DIC microscope, the boundary between layer 1 (L1) and 2 (L2) was easily distinguishable in terms of cell density. Below L2, the sparser area of neurons (L3) was followed by a tight band of densely packed layer 4 (L4) neurons, with a decrease in cell density indicating layer 5 (L5) [22, 25].

Patch pipettes (3-6 MΩ resistance) were pulled from standard borosilicate glass pipettes (thin-wall borosilicate tubes with filaments, World Precision Instruments, Sarasota, FL, USA) using a vertical puller (PC-10, Narishige). Pipettes were filled with intracellular solution containing (in mM): K-gluconate 135; NaCl 10; HEPES 10; $MgCl_2$ 1; $Na_2ATP$ 2; GTP 0.3, pH adjusted with KOH to 7.4 (290–309 mOsm). In a subset of experiments the pipette solution also contained biocytin (3-5%).

Whole-cell patch-clamp recordings were obtained using a Multiclamp 700A amplifier, Axopatch 200B amplifier, pClamp 9.2 and pClamp 10.6 data acquisition software (Axon instruments, Molecular Devices, USA). Subsequently, electrical signals were digitized at 20 kHz using a 1320X digitizer. The access resistance was monitored throughout the recording (typically between 8-25 MΩ), and neurons were discarded if the access resistance was >25 MΩ. The liquid junction potential was calculated to be -10.8 mV and was not corrected.

Electrophysiological data were analyzed off-line using Clampfit 10.7, Python and MATLAB [54]. Electrophysiological features were calculated from responses elicited by 600 ms square current steps as previously

described [22]. Briefly, the resting membrane potential (RMP) was measured after breaking into the cell (IC=0). The firing threshold was calculated following depolarizing current injections between 50 to 250 pA with 50 pA step size for 600 ms and classifying the current at which a spike was first elicited as the threshold. The distance to threshold presented in this paper was calculated as the difference between the RMP and threshold. The average FI curve (i.e., activation function) was generated by calculating the instantaneous frequency at each spike and averaging them for each of the depolarizing current injections (50-250 pA, step size 50 pA, 600 ms).

Plotting of experimental data was performed using GraphPad Prism 6 (GraphPad software, Inc, CA, USA). The non-parametric Mann-Whitney test was used to determine statistical differences between the means of two groups. The F-test was used to compare standard deviation (SD) between groups. The two sample coefficient of variation test was used to compare the coefficient of variance (CV) between groups. Normality of the data was tested with the Shapiro-Wilk and D'Agostino & Pearson omnibus normality tests with alpha=0.05. A standard threshold of $p<0.05$ is used to report statistically significant differences.

## Modeling: spiking neural network

The cortical spiking neural network contains populations of recurrently connected excitatory and inhibitory neurons [55, 56]. The spiking response of those neurons obeys the non-homogeneous Poisson process

$$Y_j \rightarrow Poisson(f(u_j, h_j)) \tag{1}$$

where $Y_j = \sum_l \delta(t - t_k)$ is a Poisson spike train with rate $f(u_j, h_j)$.

The firing rate of neuron $j$ is determined by the non-linear sigmoidal activation function $f(u_j, h_j)$,

$$f(u_j, h_j) = \frac{1}{1 + e^{-\beta(u_j - h_j)}} \tag{2}$$

where $u_j$ is the membrane potential analogue and $h_j$ represents the rheobase. The constant $\beta = 4.8$ scales the non-linear gain.

Neural heterogeneity is implemented via the addition of random rheobases $h_j$ varying between each neuron. Specifically, the $h_j$ values are chosen by independently and randomly sampling a normal Gaussian distribution whose standard deviation is $\sigma_e$ if neuron $j$ is an excitatory neuron ($x = e$) and $\sigma_i$ if neuron $j$ is an inhibitory neuron ($x = i$). The values of $\sigma_i$ and $\sigma_e$ are varied throughout these explorations between a minimum value of 2.5 mV and a maximum value of 16.75 mV. The heterogeneity parameters for the model have a direct parallel with the heterogeneity in the distance to threshold (DTT) measured experimentally,

with $\beta$ chosen so that the experimentally observed heterogeneity values and the heterogeneity parameters implemented in the model are within the same range (see Figure 2c,d).

The membrane potential $u_j$ evolves over time influenced by various inputs, both synaptic and external. The equation defining these dynamics is

$$\frac{du_j}{dt} = \alpha_x \left(-u_j(t) + Syn_j^{ex} + Syn_j^{ix} + I_x + I(t)\right) + \sqrt{2\alpha_x D} X_j \tag{3}$$

The variable $\alpha_x$ represents the time constant depending upon whether the neuron $j$ is excitatory ($x = e, \alpha_e = 10$ ms) or inhibitory ($x = i, \alpha_i = 5$ ms). The differential time scales are implemented in consideration of the differential membrane time constants between cortical pyramidal neurons and parvalbumin positive (PV) interneurons [31].

$Syn_j^{ex}$ and $Syn_j^{ix}$ are the synaptic inputs to the cell $j$ (from the excitatory and inhibitory populations, respectively), dependent upon whether cell $j$ is excitatory ($x = e$) or inhibitory ($x = i$). Our cortical model is built of 800 excitatory and 200 inhibitory neurons [57–59]. The connectivity density for each connection type (E-E, E-I, I-E, and I-I) is varied uniformly via a parameter $p$. In this study, $p = 1$ is used unless otherwise noted ($p = 0.25, 0.5,$ and $0.75$ are examined in Supplementary Figure S2) . The strength of the synaptic connections vary depending upon the type of connection and are represented by the variables $w_{xy}$ where $x, y = e, i$ depending upon whether the pre-synaptic cell ($x$) and the post-synaptic cell ($y$) are excitatory or inhibitory. In our model, $w_{ee} = 100.000$, $w_{ei} = 187.500$, $w_{ie} = -293.750$, and $w_{ii} = -8.125$. Here, negative signs represent inhibitory signalling (i.e. the pre-synaptic cell is an inhibitory cell), while positive signs represent excitatory signalling (i.e. the pre-synaptic cell is an excitatory cell). These values are chosen to place the network near a bifurcation between asynchronous and synchronous firing based on mathematical analysis and previous modeling work [32], and scaled relative to the values of $\beta$.

The post-synaptic inputs $Syn_j^{ex}$ and $Syn_j^{ix}$ are given by

$$Syn_j^{ex} = \frac{1}{800} \sum_{k=1, k\neq j}^{800} c_{kj} \frac{w_{ex}}{p} Y_k(t - \Delta t) \tag{4}$$

$$Syn_j^{ix} = \frac{1}{200} \sum_{k=1, k\neq j}^{200} c_{kj} \frac{w_{ix}}{p} Y_k(t - \Delta t) \tag{5}$$

where $x = e, i$ and $Y_k$ is a Poisson spike train given by $Y_k = \sum_l \delta(t - t_l)$. The connectivity scheme excludes the possibility of an auto-synapse. The term $c_{kj}$ represents the connectivity: if neuron $k$ synapses onto neuron $j$, $c_{kj} = 1$, and otherwise $c_{kj} = 0$. Note that the synaptic weights are scaled by the connectivity density $p$ so

that the net input signal to each neuron is not affected by the number of connections.

Equation 3 includes three non-synaptic inputs to the neuron: $I_x$, $I(t)$, and and $\sqrt{2\alpha_x D}X_j$. The variable $X_j$ is a spatially independent Gaussian white noise process. The value of noise intensity was chosen so that the noise-induced fluctuations are commensurate with endogenous dynamics of the network. $I_x$ represents a bias current whose value depends on whether the neuron is excitatory ($x = e$) or inhibitory ($x = i$), imparting a differential baseline spiking rate to these distinct populations. In this work, $I_i = -31.250$, which ensures that inhibitory neurons will require excitatory input to fire in most cases, matching intuition gleaned from the biophysical setting. Meanwhile, the baseline value of $I_e = -15.625$ is based on previous literature [29–32] to position the system near the transition between asynchronous and synchronous firing.

$I(t)$ implements time-varying external input to the neurons, and is only applied to the excitatory population (this is simply referred to as the "drive" to the system in Figures 2, 3 and 4). In this work, this term is used primarily to study the response of the spiking network to a linear ramp excitatory input that occurs at a time scale much slower than the dynamics of individual neurons: to yield the ramp current used throughout the study $I(t)$ simply varies linearly between 0 and 31.25 over a 2500 ms simulation. In Figure 5 where we characterize the dynamics of the network with constant input, $I(t) = 15.625$ uniformly.

The final probability of a Poisson neuron $j$ firing at time $t$ depends upon the effect of these various elements on $u_j$:

$$\rho_j = 1 - e^{-f(u_j(t),h_j)dt} \tag{6}$$

## Parameter values

Parameter values dictating the features of this spiking network are summarized in Table 1 below. These values are analogous to those used in previous work on oscillatory cortical networks [29–32] with the scaling of our chosen $\beta$ taken into account.

## Numerics

All sampling from standard normal Gaussian distributions is done via the Box-Mueller algorithm [60]. Equations are integrated using the Euler-Maruyama method. In our simulations, $\Delta t = 0.1$, which we scale so that each time step $\Delta t$ represents 1 ms.

The excitatory network synchrony (i.e. Synchrony Measure) and excitatory and inhibitory firing rates are calculated over sliding 100 ms time windows in Figures 2, 3 and 4. To preserve symmetry and ensure initial transients do not skew the data, our first window begins at $t = 100$.

The Synchrony Measure is an adaptation of a commonly used measure developed by Golomb and Rinzel [61, 62] to quantify the degree of coincident spiking in a network. This particular implementation of

this measure has been utilized in our previous studies [34, 58, 59, 63]. Briefly, the measure involves convolving a very narrow Gaussian function with the time of each action potential for every cell to generate functions $V_i(t)$. The population averaged voltage $V(t)$ is then defined as $V(t) = \frac{1}{N}\sum_{i=1}^{N} V_i(t)$, where $N$ is the number of cells in the network. The overall variance of the population averaged voltage $\mathrm{Var}(V)$ and the variance of an individual neuron's voltage $\mathrm{Var}(V_i)$ is defined as

$$\mathrm{Var}(V) =< V(t)^2 > - < V(t) >^2 \tag{7}$$

and

$$\mathrm{Var}(V_i) =< V_i(t)^2 > - < V_i(t) >^2 \tag{8}$$

where $< \cdot >$ indicates time averaging over the interval for which the measure is taken. The Synchrony Measure $S$ is then defined as

$$S = \frac{\mathrm{Var}(V)}{\frac{1}{N}\sum_{i=1}^{N} \mathrm{Var}(V_i)} \tag{9}$$

The value $S = 0$ indicates completely asynchronous firing, while $S = 1$ corresponds to fully synchronous network activity. Intermediate values represent intermediate degrees of synchronous firing. We note that the Synchrony Measure is only calculated for excitatory neurons considering these cells are generally considered to dictate the output of a particular neural circuit.

In the case of sliding time bins, this measure is taken by simply only considering spikes falling into the time window of interest. In contrast, in Figure 5**(b-e)** we generate a single value the Synchrony Measure (or the other measures of interest) over the last 1000 ms of the simulation. We also calculate the Mean Firing Frequency (MFF) simply by summing the total number of excitatory spikes over the last 1000 ms, dividing by the number of excitatory neurons (800), and then converting this into a frequency by dividing by the time frame (1 second). Figure 5**(b-e)** displays these measures averaged over five independent simulations.

Figure 5 also includes the presentation of our Bifurcation Measure $B$. This measure quantifies the presence of any period of sudden and significant changes in the Synchrony Measure over time. This measure is calculated via a simple three step process: first, the Synchrony Measure time series (i.e. as presented in Figure 3) is "smoothed" simply using the *smooth* function in MATLAB [54] with a 500 step window (serving to mitigate the impact of variability in the Synchrony Measure caused by the relatively small time window relative to the oscillatory frequency, and also indirectly "fit" more linear functions to the qualitatively different portions of the curve); second, the derivative is approximated at each time step using a difference

quotient, where the "x" variable is the external input to the excitatory population; third, the variance of these derivative values is calculated using the *var* function in MATLAB [54]. The final values presented in the heatmap in Figure 5**(a)** as well as in Supplementary Figure S2 are averages of $B$ taken over 10 independent simulations.

### Analysis of FI curves

In Figure 6, we compare activation functions derived from experimental data with the analogue in our models, which is the function $F$ described below in Equation 12. In Figure 6**(b)** we show examples of the $F$ function with epileptogenic and non-epileptogenic levels of heterogeneity alongside samples of the function $f$ (Equation 2) randomly chosen based on the differing heterogeneity levels, illustrating how the differences in the two $F$ curves arise by averaging the effects of the individual $f$ curves.

While our experimentally derived values of $\sigma_e$, when implemented in the corresponding function $F$, yield close qualitative fits to the experimental data shown in Figure 6**(a)**, we confirmed this by determining the value of $\sigma_e$ that best fit this data. This process involved three steps: first, we qualitatively determined the portion of the $F$ curves most likely to fit this data as that in $-11.875 \leq U_e \leq -6.25$; second, both the x ($U_e$, [-11.875 -6.25]) and y (probability of firing, [0.003585 .2118]) variables were re-scaled to match the ranges exhibited by the x (input current, pA, [50 250]) and y (firing frequency, Hz, [0 24]) variables in the experimental data; finally, a fit was calculated using MATLAB's [54] Curve Fitting application. This process used a non-linear least squares method, with $r^2 > .93$ for both fits (see details in Results). Additional scaling was performed for plotting so that the two x- and y-axes in Figure 6 remain consistent.

## Mean-field reduction

Following the lines of previous work [32, 38, 64–67] we perform a mean-field reduction of the spiking network in Equation 3. We assume that the firing rate of cells is sufficiently high to make use of the diffusion approximation [68], yielding

$$\alpha_e^{-1}\frac{dU_e}{dt} = -U_e + w_{ee}F(U_e,\sigma_e) + w_{ie}F(U_i,\sigma_i) + I^e \tag{10}$$

$$\alpha_i^{-1}\frac{dU_i}{dt} = -U_i + w_{ii}F(U_i,\sigma_i) + w_{ei}F(U_e,\sigma_i e) + I^i \tag{11}$$

where $U_{e,i} = \sum_{j=1}^{N_{e,i}} u_{e,i}^j$ represents the mean activity of the excitatory or inhibitory population, respectively.

The function $F$ represents the average activation function of the neural populations conditioned upon the

value of $\sigma_{e,i}$ via the convolution

$$F(U_{e,i}, \sigma_{e,i}) = \int_{-\infty}^{\infty} f(U_{e,i} + v, 0)\rho(v, \sigma_{e,i})dv \tag{12}$$

where $\rho(v, \sigma_{e,i}) = N(0, \sigma_{e,i}^2)$ [38, 64, 69].

### Linear stability analysis of the mean-field equations

Fixed points $\bar{U}_{e,i}$ of the mean-field equations satisfy

$$0 = -\bar{U_e} + w_{ee}F(\bar{U_e}, \sigma_e) + w_{ie}F(\bar{U_i}, \sigma_i) + I^e \tag{13}$$

$$0 = -\bar{U_i} + w_{ii}F(\bar{U_i}, \sigma_i) + w_{ei}F(\bar{U_e}, \sigma_i e) + I^i \tag{14}$$

Linearizing about the steady state values of $\bar{U_{e,i}}$ yields the system

$$\mathbf{A}\begin{pmatrix} \delta\bar{U_e} \\ \delta\bar{U_i} \end{pmatrix} = \begin{pmatrix} -1 + w_{ee}\alpha_e R^e & w_{ie}\alpha_i R^i \\ w_{ei}\alpha_e R^e & -1 + w_{ii}\alpha_i R^i \end{pmatrix}\begin{pmatrix} \delta\bar{U_e} \\ \delta\bar{U_i} \end{pmatrix} \tag{15}$$

with $R^{e,i} = R(\bar{U_e}, \bar{U_i}) = \int_{\Omega(v)} f'[\bar{U}_{e,i} + v, 0]\rho(v, \sigma_{e,i})dv$. The stability of this system is given by the eigenvalues of the Jacobian $\mathbf{A}$. We define

$$B = \text{trace}(\mathbf{A}) = -\left(-2 + (w_{ee}\alpha_e)\, R^e + (w_{ii}\alpha_i)\, R^i\right) \tag{16}$$

$$C = \det(\mathbf{A}) = (-1 + (w_{ee}\alpha_e)\, R^e)\left(-1 + (w_{ii}\alpha_i)\, R^i\right) - \left((w_{ie}\alpha_i)\, R^i\right)((w_{ei}\alpha_e)\, R^e) \tag{17}$$

Eigenvalues of $\mathbf{A}$ are thus given by

$$\lambda_{\pm} = \frac{-B \pm \sqrt{B^2 - 4C}}{2} \tag{18}$$

### Bifurcation analysis with varying excitatory input

We investigate the bifurcation properties of this system as a function of $I^e$. In Figure 5**(a)**, multi-stability, as denoted by the bold border, is determined by testing for the presence of multiple fixed points at input currents ranging from -15.625:0.625:-6.250, a range encompassing the range for multi-stability shown in Figure 4.

## Code Accessibility

The code/software described in the paper is freely available upon request to the authors.

# References


[1] Reynolds, E. H. Introduction: epilepsy in the world. *Epilepsia* **43**, 1–3 (2002).

[2] Jiruska, P. *et al.* Synchronization and desynchronization in epilepsy: controversies and hypotheses. *The Journal of physiology* **591**, 787–797 (2013).

[3] Noebels, J. L., Avoli, M., Rogawski, M. A., Olsen, R. W. & Delgado-Escueta, A. V. Jasper's basic mechanisms of the epilepsies [internet] (2012).

[4] Jirsa, V. K., Stacey, W. C., Quilichini, P. P., Ivanov, A. I. & Bernard, C. On the nature of seizure dynamics. *Brain* **137**, 2210–2230 (2014).

[5] Saggio, M. L. *et al.* A taxonomy of seizure dynamotypes. *Elife* **9**, e55632 (2020).

[6] Dehghani, N. *et al.* Dynamic balance of excitation and inhibition in human and monkey neocortex. *Scientific reports* **6**, 1–12 (2016).

[7] Žiburkus, J., Cressman, J. R. & Schiff, S. J. Seizures as imbalanced up states: excitatory and inhibitory conductances during seizure-like events. *Journal of neurophysiology* **109**, 1296–1306 (2013).

[8] Renart, A. *et al.* The asynchronous state in cortical circuits. *science* **327**, 587–590 (2010).

[9] Mishra, P. & Narayanan, R. Disparate forms of heterogeneities and interactions among them drive channel decorrelation in the dentate gyrus: Degeneracy and dominance. *Hippocampus* **29**, 378–403 (2019).

[10] Altschuler, S. J. & Wu, L. F. Cellular heterogeneity: do differences make a difference? *Cell* **141**, 559–563 (2010).

[11] Marder, E. & Goaillard, J.-M. Variability, compensation and homeostasis in neuron and network function. *Nature Reviews Neuroscience* **7**, 563 (2006).

[12] Padmanabhan, K. & Urban, N. N. Intrinsic biophysical diversity decorrelates neuronal firing while increasing information content. *Nature neuroscience* **13**, 1276 (2010).

[13] Tripathy, S. J., Padmanabhan, K., Gerkin, R. C. & Urban, N. N. Intermediate intrinsic diversity enhances neural population coding. *Proceedings of the National Academy of Sciences* **110**, 8248–8253 (2013).

[14] Zhang, Z., Valiante, T. & Carlen, P. Transition to seizure: from "macro"-to "micro"-mysteries. *Epilepsy research* **97**, 290–299 (2011).

[15] Trevelyan, A. J., Bruns, W., Mann, E. O., Crepel, V. & Scanziani, M. The information content of physiological and epileptic brain activity. *The Journal of physiology* **591**, 799–805 (2013).

[16] Cossart, R. *et al.* Dendritic but not somatic gabaergic inhibition is decreased in experimental epilepsy. *Nature neuroscience* **4**, 52–62 (2001).

[17] Cobos, I. *et al.* Mice lacking dlx1 show subtype-specific loss of interneurons, reduced inhibition and epilepsy. *Nature neuroscience* **8**, 1059–1068 (2005).

[18] Arnold, E. C., McMurray, C., Gray, R. & Johnston, D. Epilepsy-induced reduction in hcn channel expression contributes to an increased excitability in dorsal, but not ventral, hippocampal ca1 neurons. *Eneuro* **6** (2019).

[19] Klaassen, A. *et al.* Seizures and enhanced cortical gabaergic inhibition in two mouse models of human autosomal dominant nocturnal frontal lobe epilepsy. *PNAS* **103**, 19152–19157 (2006).

[20] Albertson, A. J., Yang, J. & Hablitz, J. J. Decreased hyperpolarization-activated currents in layer 5 pyramidal neurons enhances excitability in focal cortical dysplasia. *Journal of neurophysiology* **106**, 2189–2200 (2011).

[21] Sutula, T. P. & Dudek, F. E. Unmasking recurrent excitation generated by mossy fiber sprouting in the epileptic dentate gyrus: an emergent property of a complex system. *Progress in brain research* **163**, 541–563 (2007).

[22] Chameh, H. M. *et al.* Sag currents are a major contributor to human pyramidal cell intrinsic differences across cortical layers. *Nature Communications, in press* (2021).

[23] Hodge, R. D. *et al.* Conserved cell types with divergent features in human versus mouse cortex. *Nature* 1–8 (2019).

[24] Beaulieu-Laroche, L. *et al.* Enhanced dendritic compartmentalization in human cortical neurons. *Cell* **175**, 643–651 (2018).

[25] Kalmbach, B. *et al.* Signature morpho-electric, transcriptomic, and dendritic properties of extratelencephalic-projecting human layer 5 neocortical pyramidal neurons. *bioRxiv* (2020).

[26] Kramer, M. A., Kirsch, H. E. & Szeri, A. J. Pathological pattern formation and cortical propagation of epileptic seizures. *Journal of the Royal Society Interface* **2**, 113–127 (2005).

[27] Vogels, T. P. & Abbott, L. Gating multiple signals through detailed balance of excitation and inhibition in spiking networks. *Nature neuroscience* **12**, 483 (2009).

[28] Ostojic, S. Two types of asynchronous activity in networks of excitatory and inhibitory spiking neurons. *Nature neuroscience* **17**, 594–600 (2014).

[29] Jadi, M. P. & Sejnowski, T. J. Cortical oscillations arise from contextual interactions that regulate sparse coding. *Proceedings of the National Academy of Sciences* **111**, 6780–6785 (2014).

[30] Jadi, M. P. & Sejnowski, T. J. Regulating cortical oscillations in an inhibition-stabilized network. *Proceedings of the IEEE* **102**, 830–842 (2014).

[31] Neske, G. T., Patrick, S. L. & Connors, B. W. Contributions of diverse excitatory and inhibitory neurons to recurrent network activity in cerebral cortex. *Journal of Neuroscience* **35**, 1089–1105 (2015).

[32] Rich, S., Hutt, A., Skinner, F., Valiante, T. & Lefebvre, J. Neurostimulation stabilizes spiking neural networks by disrupting seizure-like oscillatory transitions. *Scientific Reports* (2020).

[33] Chow, S.-N. & Hale, J. K. *Methods of bifurcation theory*, vol. 251 (Springer Science & Business Media, 2012).

[34] Rich, S. *et al.* Inhibitory network bistability explains increased interneuronal activity prior to seizure onset. *Frontiers in Neural Circuits* **13**, 81 (2020).

[35] Ferguson, K. A., Huh, C. Y., Amilhon, B., Williams, S. & Skinner, F. K. Experimentally constrained ca1 fast-firing parvalbumin-positive interneuron network models exhibit sharp transitions into coherent high frequency rhythms. *Frontiers in computational neuroscience* **7**, 144 (2013).

[36] Schevon, C. A. *et al.* Evidence of an inhibitory restraint of seizure activity in humans. *Nature communications* **3**, 1–11 (2012).

[37] Mejias, J. F. & Longtin, A. Differential effects of excitatory and inhibitory heterogeneity on the gain and asynchronous state of sparse cortical networks. *Frontiers in computational neuroscience* **8**, 107 (2014).

[38] Lefebvre, J., Hutt, A., Knebel, J.-F., Whittingstall, K. & Murray, M. M. Stimulus statistics shape oscillations in nonlinear recurrent neural networks. *Journal of Neuroscience* **35**, 2895–2903 (2015).

[39] Börgers, C. & Kopell, N. Synchronization in networks of excitatory and inhibitory neurons with sparse, random connectivity. *Neural computation* **15**, 509–538 (2003).

[40] Börgers, C. & Kopell, N. Effects of noisy drive on rhythms in networks of excitatory and inhibitory neurons. *Neural computation* **17**, 557–608 (2005).

[41] Börgers, C., Franzesi, G. T., LeBeau, F. E., Boyden, E. S. & Kopell, N. J. Minimal size of cell assemblies coordinated by gamma oscillations. *PLoS Comput Biol* **8**, e1002362 (2012).

[42] Yim, M. Y., Aertsen, A. & Rotter, S. Impact of intrinsic biophysical diversity on the activity of spiking neurons. *Physical Review E* **87**, 032710 (2013).

[43] Mejias, J. & Longtin, A. Optimal heterogeneity for coding in spiking neural networks. *Physical Review Letters* **108**, 228102 (2012).

[44] Cossart, R. The maturation of cortical interneuron diversity: how multiple developmental journeys shape the emergence of proper network function. *Current opinion in neurobiology* **21**, 160–168 (2011).

[45] Huang, Z. J. & Paul, A. The diversity of gabaergic neurons and neural communication elements. *Nature Reviews Neuroscience* **20**, 563–572 (2019).

[46] Gavrilovici, C., Pollock, E., Everest, M. & Poulter, M. O. The loss of interneuron functional diversity in the piriform cortex after induction of experimental epilepsy. *Neurobiology of disease* **48**, 317–328 (2012).

[47] Rich, S., Moradi Chameh, H., Sekulic, V., Valiante, T. A. & Skinner, F. K. Modeling reveals human–rodent differences in h-current kinetics influencing resonance in cortical layer 5 neurons. *Cerebral Cortex* **31**, 845–872 (2021).

[48] Lee, S.-A., Spencer, D. D. & Spencer, S. S. Intracranial eeg seizure-onset patterns in neocortical epilepsy. *Epilepsia* **41**, 297–307 (2000).

[49] Velascol, A. L., Wilson, C. L., Babb, T. L. & Engel Jr, J. Functional and anatomic correlates of two frequently observed temporal lobe seizure-onset patterns. *Neural plasticity* **7**, 49–63 (1999).

[50] Marder, E. Variability, compensation, and modulation in neurons and circuits. *Proceedings of the National Academy of Sciences of the United States of America* **108 Suppl 3**, 15542–15548 (2011).

[51] Fallah, A. *et al.* Anterior cervical discectomy with arthroplasty versus arthrodesis for single-level cervical spondylosis: a systematic review and meta-analysis. *PLoS One* **7**, e43407 (2012).

[52] Kostopoulos, G., Drapeau, C., Avoli, M., Olivier, A. & Villemeure, J. G. Endogenous adenosine can reduce epileptiform activity in the human epileptogenic cortex maintained in vitro. *Neuroscience letters* **106**, 119–124 (1989).

[53] Kalmbach, B. E. *et al.* h-channels contribute to divergent intrinsic membrane properties of supragranular pyramidal neurons in human versus mouse cerebral cortex. *Neuron* **100**, 1194–1208 (2018).

[54] MATLAB. *version 9.6.0 (R2019a)* (The MathWorks Inc., Natick, Massachusetts, 2019).

[55] Snyder, D. L. & Miller, M. I. *Random point processes in time and space* (Springer Science & Business Media, 2012).

[56] Stevens, C. F. & Zador, A. M. When is an integrate-and-fire neuron like a poisson neuron? In *Advances in neural information processing systems*, 103–109 (1996).

[57] Traub, R. D., Jefferys, J. G. & Whittington, M. A. Simulation of gamma rhythms in networks of interneurons and pyramidal cells. *Journal of computational neuroscience* **4**, 141–150 (1997).

[58] Rich, S., Zochowski, M. & Booth, V. Dichotomous dynamics in ei networks with strongly and weakly intra-connected inhibitory neurons. *Frontiers in neural circuits* **11**, 104 (2017).

[59] Rich, S., Zochowski, M. & Booth, V. Effects of neuromodulation on excitatory–inhibitory neural network dynamics depend on network connectivity structure. *Journal of Nonlinear Science* 1–24 (2018).

[60] Golder, E. & Settle, J. The box-müller method for generating pseudo-random normal deviates. *Journal of the Royal Statistical Society: Series C (Applied Statistics)* **25**, 12–20 (1976).

[61] Golomb, D. & Rinzel, J. Dynamics of globally coupled inhibitory neurons with heterogeneity. *Physical review E* **48**, 4810 (1993).

[62] Golomb, D. & Rinzel, J. Clustering in globally coupled inhibitory neurons. *Physica D: Nonlinear Phenomena* **72**, 259–282 (1994).

[63] Rich, S., Booth, V. & Zochowski, M. Intrinsic cellular properties and connectivity density determine variable clustering patterns in randomly connected inhibitory neural networks. *Frontiers in neural circuits* **10**, 82 (2016).

[64] Hutt, A., Mierau, A. & Lefebvre, J. Dynamic control of synchronous activity in networks of spiking neurons. *PloS one* **11** (2016).

[65] Stefanescu, R. A., Shivakeshavan, R. & Talathi, S. S. Computational models of epilepsy. *Seizure* **21**, 748–759 (2012).

[66] Hutt, A., Lefebvre, J., Hight, D. & Kaiser, H. Phase coherence induced by additive gaussian and non-gaussian noise in excitable networks with application to burst suppression-like brain signals. *Frontiers in Applied Mathematics and Statistics* (2019).

[67] Hutt, A., Lefebvre, J., Hight, D. & Kaiser, H. A. Phase coherence induced by additive gaussian and non-gaussian noise in excitable networks with application to burst suppression-like brain signals. *Frontiers in applied mathematics and statistics* **5**, 69 (2020).

[68] Gluss, B. A model for neuron firing with exponential decay of potential resulting in diffusion equations for probability density. *Bulletin of Mathematical Biophysics* **29**, 233–243 (1967).

[69] Hutt, A., Lefebvre, J., Hight, D. & Sleigh, J. Suppression of underlying neuronal fluctuations mediates EEG slowing during general anaesthesia. *Neuroimage* **179**, 414–428 (2018).

# Figure Legends

Figure 1: ***In vitro* human tissue recordings reveal significantly different electrophysiological heterogeneity between epileptogenic and non-epileptogenic populations**. **(a)**: The coefficient of variation (CV) in the distance to threshold (DTT) is significantly larger in both non-epileptogenic MTG and non-epileptogenic (tumor) frontal lobe compared to epileptogenic frontal lobe (p=0.04 to non-epileptogenic MTG, p=0.03 to non-epileptogenic frontal, two sample coefficient of variation test). The CV measure is implemented considering the significantly reduced mean DTT in non-epileptogenic frontal lobe compared to the other two populations (p=0.01 for both comparisons, non-parametric Mann-Whitney test). We compare epileptogenic frontal lobe and non-epileptogenic MTG computationally given their similar mean DTT (p=0.7, non-parametric Mann-Whitney test). Plotted bars indicate mean ± SD. **(b)**: An alternative visualization of the DTT distributions via fit Gaussian probability density functions. All three data sets were deemed normal after passing both the Shapiro-Wilk and D'Agostino & Pearson omnibus normality test with alpha=0.05. **(c)**: Neurons from non-epileptogenic populations show similar, linear activation functions (i.e., FI curves). There are significant differences between the firing frequencies for a 200 pA injection between epileptogenic frontal lobe and non-epileptogenic MTG (p=0.009; two-way ANOVA-Tukey's multiple comparison test) and between

epileptogenic frontal lobe and non-epileptogenic frontal lobe (p=0.03; two-way ANOVA-Tukey's multiple comparison test), as well as for a 250 pA injection between epileptogenic frontal lobe and non-epileptogenic MTG (p=0.002; two-way ANOVA-Tukey's multiple comparison test) and between epileptogenic frontal lobe and non-epileptogenic frontal lobe (p=0.02; two-way ANOVA-Tukey's multiple comparison test). Plotted bars indicate mean ± standard error measure (SEM).

Figure 2: **Experimentally observed decreases in heterogeneity amongst excitatory cells promote epileptogenic-like transitions in E-I spiking neural network models**. **(a-b)**: Schematic representation of model spiking E-I networks, with pyramidal neurons represented as triangles and interneurons as circles. Blue neurons represent non-epileptogenic (i.e. high) levels of heterogeneity (as also seen in the variable neuron sizes) while red neurons represent epileptogenic (i.e. low) levels of heterogeneity (as also seen by the similar neuron sizes). This color schema is maintained in the remaining figures. Here, the inhibitory (black neurons) heterogeneity is set at a moderate value amongst the range studied ($\sigma_i = 10.0$ mV), while $\sigma_e = 7.8$ mV in panel **(a)** and $\sigma_e = 4.4$ mV in panel **(b)**. **(c-d)**: Visualizations of the distribution of model rheobases, with the solid curve (red or blue for excitatory neurons, black for inhibitory neurons) illustrating the exact Gaussian function and the corresponding histogram illustrating the example random distribution underlying the simulations presented in this figure. **(e-f)**: Example simulations with a linearly increasing excitatory drive. Background: raster plot of network activity, with each circle representing the firing of an action potential of the associated neuron (excitatory neurons below horizontal line, inhibitory neurons above). Foreground: quantifications of network activity taken over 100 ms sliding time windows, with the excitatory synchrony quantified by the Synchrony Measure in blue or red (left axis) depending on the excitatory heterogeneity level, as well as excitatory (black) and inhibitory (grey) population firing rates (right axis) Bottom: drive ($I(t)$) to the excitatory population.

Figure 3: **Effects of varied inhibitory heterogeneity on sudden transitions into synchrony in E-I spiking neural network models**. Schematics and single simulation visualizations following the conventions of Figure 2 (with inhibitory heterogeneity reflected by darker shaded blue and red neurons), now shown for four combinations of excitatory and inhibitory heterogeneities: $\sigma_e = 7.8$ mV and $\sigma_i = 2.5$ mV in panel **(a)**, $\sigma_e = 7.8$ mV and $\sigma_i = 16.75$ mV in panel **(b)**, $\sigma_e = 4.4$ mV and $\sigma_i = 2.5$ mV in panel **(c)**, and $\sigma_e = 4.4$ mV and $\sigma_i = 16.75$ mV in panel **(d)**. Relative sizes of $\sigma_e$ and $\sigma_i$ represent the relative heterogeneity levels. Sudden and simultaneous transitions into high levels of excitatory synchrony and activity are seen only in panel **(c)**, the case with low excitatory and inhibitory heterogeneities. A distinct transition into high excitatory synchrony that is not associated with a sudden increase in excitatory firing rate is seen in panel **(d)**. Meanwhile, changes in the dynamics of panels **(a)** and **(b)** are largely linear, with the excitatory synchrony

consistently lower when both excitatory and inhibitory heterogeneities are at their highest in panel **(b)**.

Figure 4: **Effects of heterogeneity on spiking network dynamics is explained by stability analysis of related mean-field equations**. Panels correspond to heterogeneity levels studied in Figure 3. Top row: measures of spiking network dynamics (as seen in Figures 2 and 3) averaged over ten simulations (dark curve=mean, lighter curve=$\pm$ one standard deviation) show the patterns seen in Figure 3 are illustrative of the general dynamics of these networks. Remaining rows: results of stability analysis on mean-field equations corresponding with these networks visualized via the fixed point of mean excitatory activity (top), and the dampening rate (i.e., the real components of the eigenvalues, middle) and oscillatory frequency (i.e., the imaginary components of the eigenvalues, bottom) associated with each fixed point. Colors represent the classification of the associated fixed point: green=saddle (one positive and one negative dampening rate value), gold=sink (two negative dampening rate values), purple=unstable oscillator (positive dampening rate value associated with an oscillation), black=stable oscillator (negative dampening rate value associated with an oscillation). Notably, only in panel **(c)**, where both heterogeneity levels are low, do we see multiple fixed points and a unique bifurcation occurring at a value of the excitatory drive corresponding to the sudden transition in the spiking networks.

Figure 5: **Exploration of a larger $\sigma_e$ and $\sigma_i$ parameter space highlights the asymmetric effects of excitatory and inhibitory heterogeneity on sudden transitions into synchrony**. **(a)**: Visualization quantifying the tendency for spiking networks to undergo a sudden and notable increase in excitatory synchrony over time, when subjected to a linearly increasing input as in Figures 2, 3 and 4, via the Bifurcation Measure $B$. Results are shown averaged over 10 independent simulations. Bold border demarcates networks whose mean-field analogues exhibit any multi-stability (bottom-left) from those that do not (top-right). **(b-c)**: Dynamics of spiking networks with a constant external input ($I(t) = 15.625$) at a baseline value where either synchronous or asynchronous activity can arise. The excitatory synchrony is quantified via the Synchrony Measure in panel **(b)** and the excitatory firing rate is quantified via the Excitatory Mean Firing Frequency in panel **(c)**. Each measure is taken over the final 1000 ms of a 2048 ms simulation, and the presented value is averaged over five independent simulations. In each of these panels, a bold border demarcates networks whose mean-field analogues have an unstable oscillator (bottom-left) from those that have a stable oscillator (top-right) as their lone fixed point when $I(t) = 15.625$.

Figure 6: **Differing levels of neural heterogeneity explain population activation function differences observed experimentally between epileptogenic and non-epileptogenic cortex**. **(a)**: Experimentally observed firing frequencies plotted against input current (left and bottom axes, mean $\pm$ SEM) for epileptogenic frontal lobe (red) and non-epileptogenic MTG (blue) tissue (as shown previously

in Figure 1**(c)**), visualized against an analogous measure of the relationship between population activity (firing probability) and drive (membrane potential analogue) in our neuron models (right and top axes, details in Methods). The shape of the curve for the heterogeneity value derived from epileptogenic tissue experimentally (red, $\sigma_e = 4.4$) qualitatively matches the experimental data, and a best fit (light red, $\sigma_e = 5.03$, $r^2$=0.9363) is obtained with a similarly low heterogeneity value. In contrast, the curve associated with the heterogeneity value derived from non-epileptogenic tissue experimentally (blue, $\sigma_e = 7.8$) closely matches the experimental data from non-epileptogenic tissue and is nearly identical to the best fit (light blue, $\sigma_e = 7.77$, $r^2$=.9840). This illustrates that increased neural heterogeneity serves to linearize input-output relationships, both experimentally and theoretically. **(b)**: A visualization of the entirety of the sigmoidal input-output relationship for our neuron models, with the regime compared to experimental data in panel **(a)** highlighted in grey. Fainter curves represent input-output relationships for individual neurons, either epileptogenic (red) or non-epileptogenic (blue): the wider variability in the blue curves yields the flatter sigmoid representing the population activation function for our non-epileptogenic heterogeneity value, and vice-versa for the red curves associated with the epileptogenic heterogeneity value.

# Figures

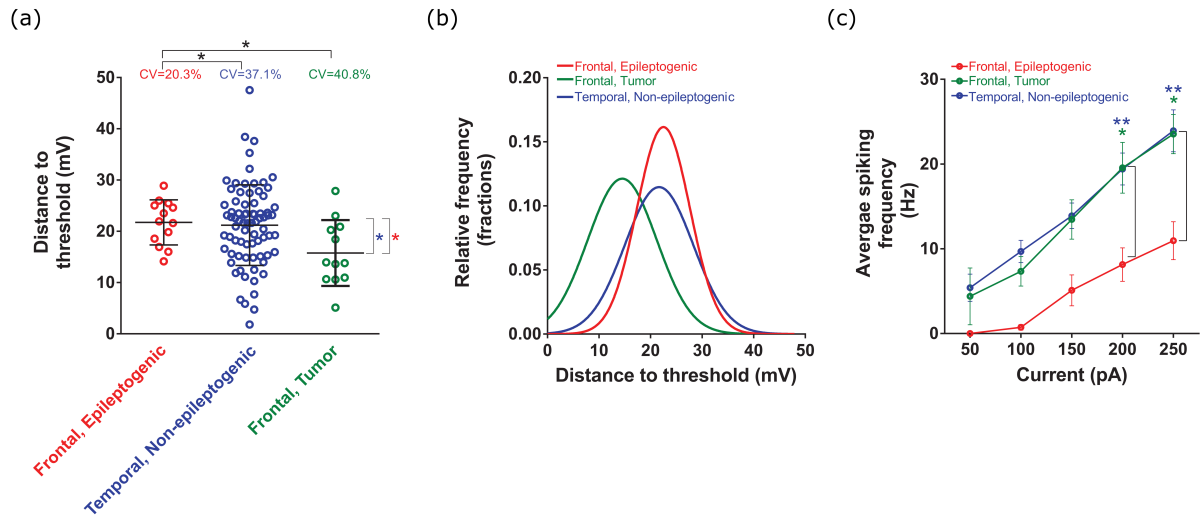


**Figure 1**

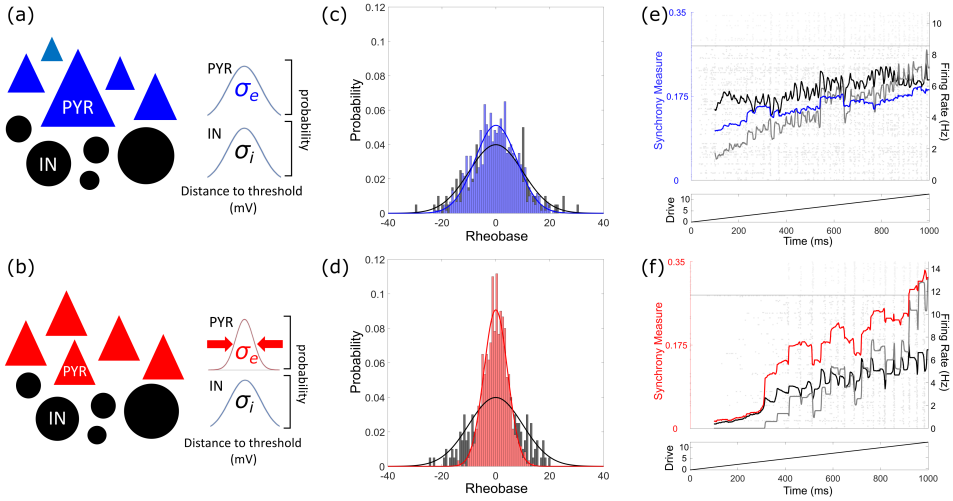


**Figure 2**

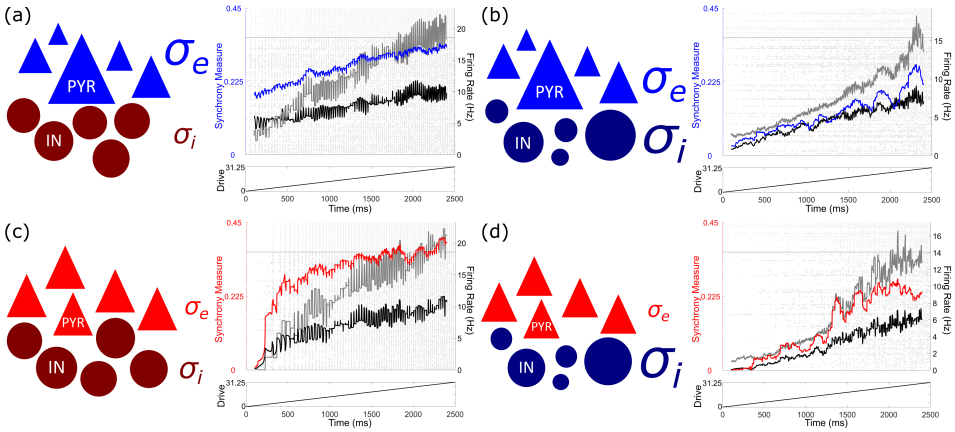
(a)
PYR
IN
$\sigma_e$
$\sigma_i$
(b)
PYR
IN
$\sigma_e$
$\sigma_i$
(c)
PYR
IN
$\sigma_e$
$\sigma_i$
(d)
PYR
IN
$\sigma_e$
$\sigma_i$
Synchrony Measure
Firing Rate (Hz)
Drive
Time (ms)

**Figure 3**

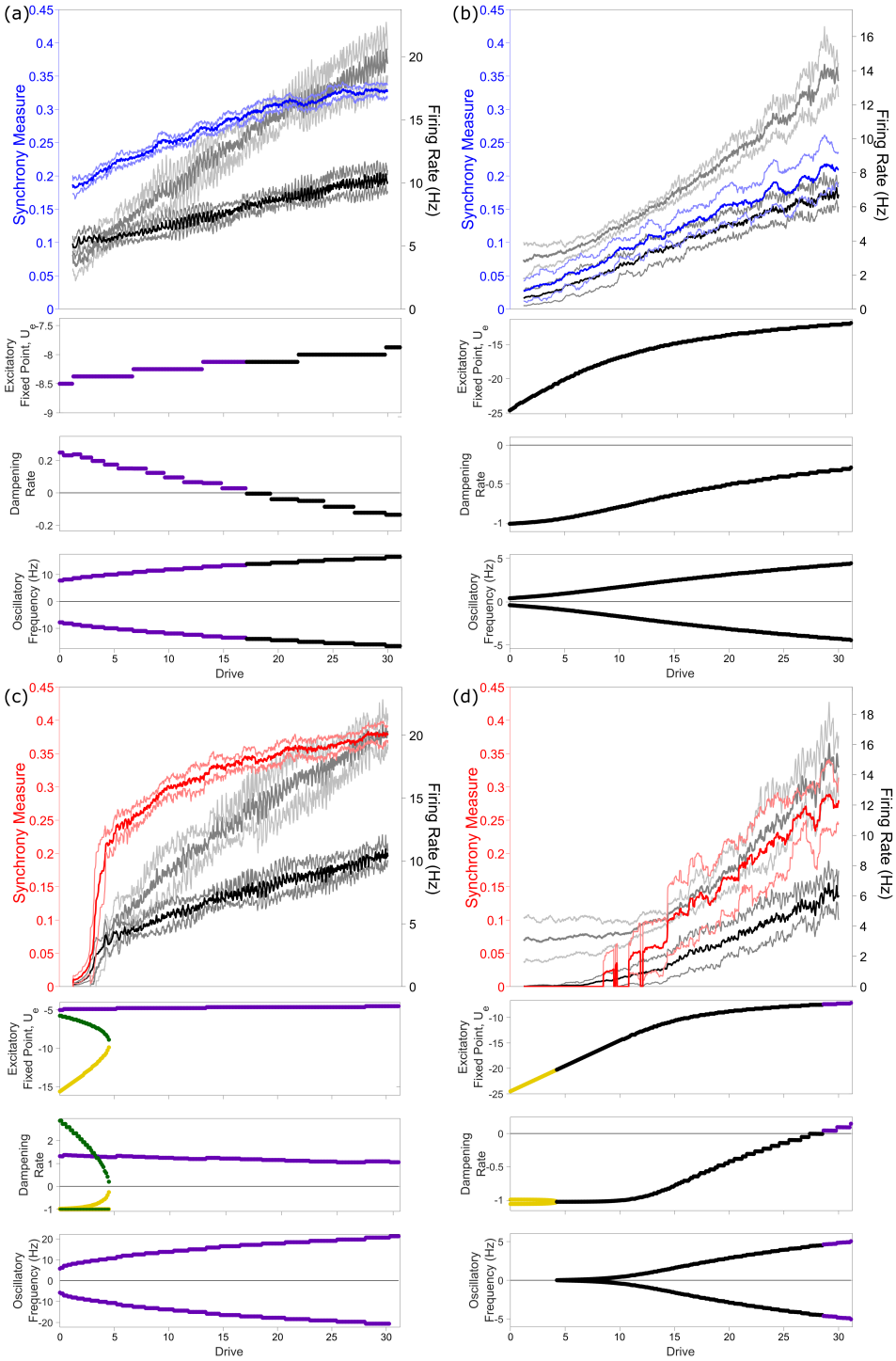
(a)
(b)
(c)
(d)
Synchrony Measure
Firing Rate (Hz)
Excitatory Fixed Point, $U_e$
Dampening Rate
Oscillatory Frequency (Hz)
Drive

**Figure 4**

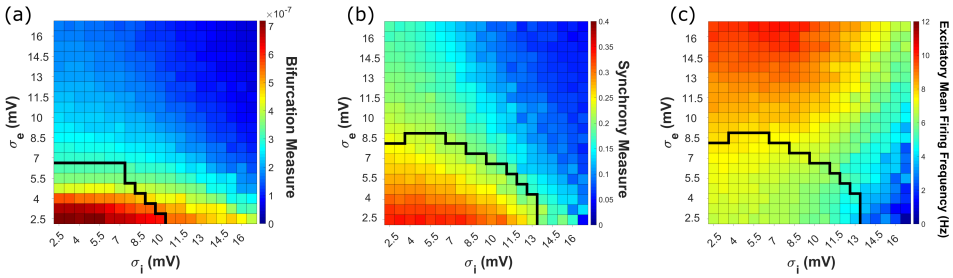


**Figure 5**

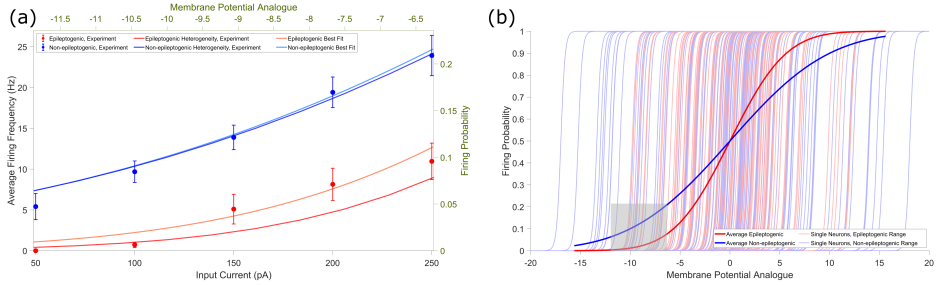


**Figure 6**

# Tables

**Table 1.** Key parameters involved in the implementation of the model.

| **Parameter** | **Value** |
|---|---|
| Number of excitatory neurons | 800 |
| Number of inhibitory neurons | 200 |
| Excitatory time constant, $\alpha_e$ | 10 ms |
| Inhibitory time constant, $\alpha_i$ | 5 ms |
| Non-linear gain of activation function, $\beta$ | 4.8 |
| Variance of noisy input, $D$ | 3.906 |
| Excitatory bias current, $I_e$ | -15.625 |
| Inhibitory bias current, $I_i$ | -31.250 |
| External input, $I(t)$ | Variable |
| Excitatory-excitatory synaptic strength, $w_{ee}$ | 100.000 |
| Excitatory-inhibitory synaptic strength, $w_{ei}$ | 187.500 |
| Inhibitory-inhibitory synaptic strength, $w_{ii}$ | -293.750 |
| Inhibitory-excitatory synaptic strength, $w_{ie}$ | -8.125 |
| Excitatory heterogeneity, $\sigma_e$ | Variable |
| Inhibitory heterogeneity, $\sigma_i$ | Variable |
| rheobase, $h$ | Variable |
| Connectivity density, $p$ | Variable |
| Time step, $\Delta t$ | 1 ms |

# Supplementary Figures

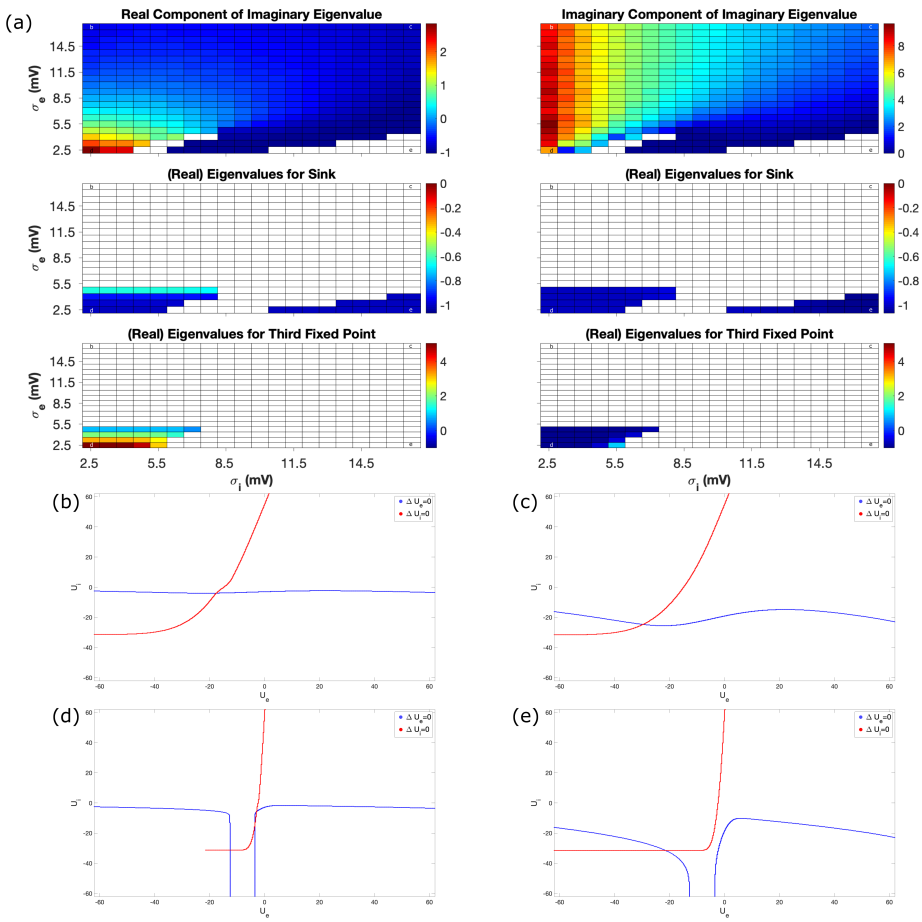


**Figure S1. Fixed points and eigenvalues of mean-field equations for $I(t) = 3.125$. (a)**: The mean-field equations with this example drive sometimes yield multiple fixed points; we calculate their eigenvalues, sort them by their classifications, and visualize these eigenvalues via heatmaps. In this example, we see that multiple fixed points arise only when both $\sigma_e$ and $\sigma_i$ are low (i.e. the bottom-left of the heatmap). **(b-e)**: Fixed points are determined by finding the intersections of the $U_e$ and $U_i$ nullclines, visualized for the corners of our heatmap (top-left in panel **(b)**, top-right in panel **(c)**, bottom-left in panel **(d)**, and bottom-right in panel **(e)**). Multiple fixed points correspond with multiple intersections of these curves, as seen exclusively in panel **(d)**.

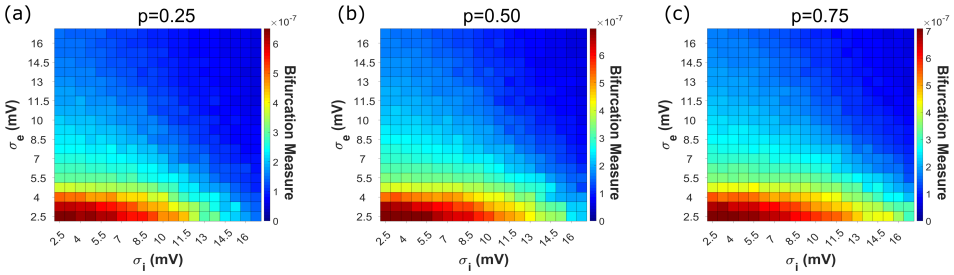


**Figure S2. Dynamics of spiking networks are robust to more sparse connectivity paradigms.** Bifurcation Measure $B$ pattern over our parameter space remains largely similar with $p = 0.25$ (panel **(a)**), $p = 0.50$ (panel **(b)**), and $p = 0.75$ (panel **(c)**), when compared to the case of $p = 1.00$ seen in Figure 5**(a)**. In each case the "asymmetry" in the effects of $\sigma_e$ and $\sigma_i$ are preserved, with the most notable differences being that the region of high $B$ shrinks slightly as $p$ decreases. Heatmaps present results averaged over ten independent simulations.

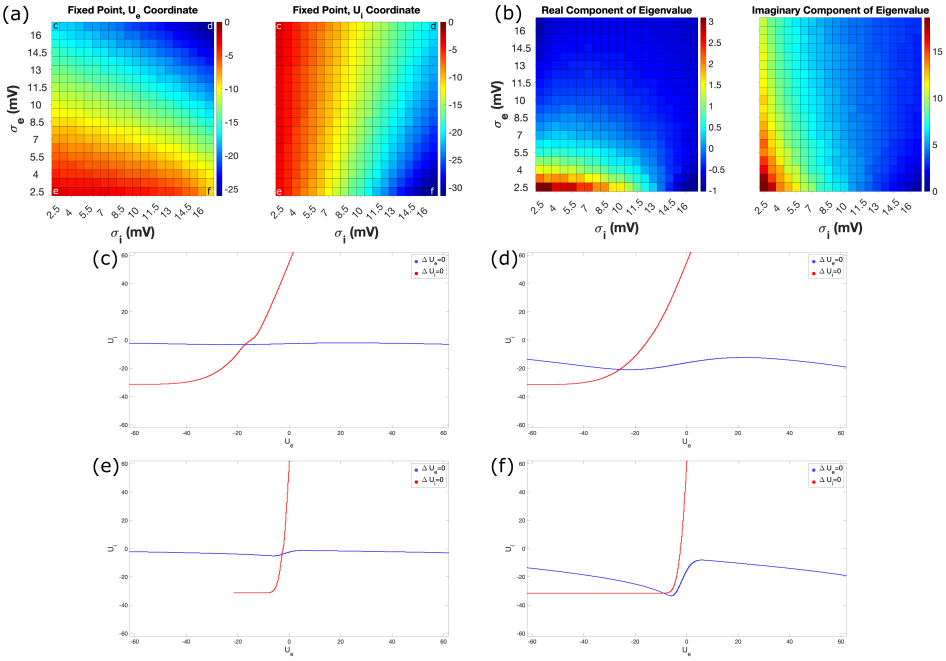


**Figure S3. Fixed points and eigenvalues of mean-field equations for $I(t) = 15.625$. (a)**: As all mean-field systems in our parameter space yield a single fixed point when $I(t) = 15.625$, we visualize the $U_e$ and $U_i$ coordinates of this fixed point using a heatmap. **(b)**: Each fixed point is classified as an oscillator, which we visualize by plotting the real and imaginary components of the eigenvalue associated with the fixed point in a heatmap. **(c-f)**: Fixed points are determined by finding the intersections of the $U_e$ and $U_i$ nullclines, visualized for the corners of our heatmap (top-left in panel **(c)**, top-right in panel **(d)**, bottom-left in panel **(e)**, and bottom-right in panel **(f)**).